

BIOENGINEERING

Fluid assessment in dialysis patients by point-of-care magnetic relaxometry

Lina A. Colucci^{1,2}, Kristin M. Corapi³, Matthew Li^{1,2}, Xavier Vela Parada³, Andrew S. Allegretti³, Herbert Y. Lin³, Dennis A. Ausiello³, Matthew S. Rosen^{4,5}, Michael J. Cima^{2,6*}

Copyright © 2019
The Authors, some
rights reserved;
exclusive licensee
American Association
for the Advancement
of Science. No claim
to original U.S.
Government Works

Magnetic resonance imaging (MRI) is a powerful diagnostic tool, but its use is restricted to the scanner suite. Here, we demonstrate that a bedside nuclear magnetic resonance (NMR) sensor can assess fluid status changes in individuals at a fraction of the time and cost compared to MRI. Our study recruited patients with end-stage renal disease (ESRD) who were regularly receiving hemodialysis treatments with intradialytic fluid removal as a model of volume overload and healthy controls as a model of euvoolemia. Quantitative T_2 measurements of the lower leg of patients with ESRD immediately before and after dialysis were compared to those of euvolemic healthy controls using both a 0.28-T bedside single-voxel NMR sensor and a 1.5-T clinical MRI scanner. In the MRI data, we found that the first sign of fluid overload was an expanded muscle extracellular fluid (ECF) space, a finding undetectable at this stage using physical exam. A decrease in muscle ECF upon fluid removal was similarly detectable with both the bedside sensor and MRI. Bioimpedance measurements performed comparably to the bedside NMR sensor but were generally worse than MRI. These findings suggest that bedside NMR may be a useful method to identify fluid overload early in patients with ESRD and potentially other hypervolemic patient populations.

INTRODUCTION

End-stage renal disease (ESRD) is associated with shortened life expectancy, despite intensive treatments such as hemodialysis (HD) (1, 2). The kidneys play an integral role in maintaining euvoolemia, and patients with ESRD, even those who undergo thrice weekly HD for the purposes of removing toxins and excess fluid, are often plagued by chronic volume overload (3). Underestimates of the fluid removal target during HD leave patients with ESRD prone to chronic volume overload, hypertension, and heart failure (1, 4–6), whereas excessive fluid removal leads to hypotension, muscle cramping, and subclinical ischemia (4–6). Both scenarios are associated with morbidity and mortality (6). A primary goal of HD is to bring patients with ESRD to their dry weight, the weight at which their extracellular volume is optimized. Determining a patient's true dry weight, however, is challenging (6). There are no accurate, objective, and noninvasive methods to monitor fluid status and determine whether a patient's extracellular volume is physiologic (5, 7, 8). The gold standard method includes a combination of subjective measurements, such as estimating the degree of lower-extremity edema (swelling) through palpation, and measurements subject to confounding, such as body weight change (5, 9–11). Nephrologists need better methods to monitor the volume status of their patients and inform their dialysis prescriptions.

A quantitative sensor to detect volume overload would benefit patient populations beyond simply those with ESRD. More than 6 million patients in the United States suffer from acute (sepsis or postsurgical) or chronic (congestive heart failure) fluid overload (12–14). Managing hypervolemia and its complications costs the U.S. health care system more than \$35 billion annually (3, 15, 16).

Bioimpedance (BI) is a noninvasive technology used for fluid assessment. BI uses skin surface electrodes to deliver multifrequency, low current into the body (17, 18). The more fluid that is present, the less resistance the current encounters when traversing the body (18). The challenge for BI is that many factors, such as body geometry and skin properties, also affect resistance (5, 19). BI accounts for these multiple factors by developing population-specific equations to correlate the measured resistance (and reactance) to fluid volumes. One of the limitations of BI is that it does not work well when applied to patients outside of the population on which the predictive algorithms were developed (20).

Nuclear magnetic resonance (NMR) relaxometry, on the other hand, provides a direct, noninvasive measurement of fluid volume and its environment (21). Quantitative magnetic resonance imaging (MRI) relaxometry is more reliable than BI when measuring muscle hydration; however, it is impractical for routine use because MRI has limited availability and is restricted to use within the scanner suite (22). Portable NMR sensors can perform the same quantitative measurements as MRI scanners while also being convenient for routine use. A variety of portable NMR sensor designs exist, many of which are single sided (also known as unilateral, strayfield, or inside-out NMR), which enables the magnet to be placed on the surface of the sample instead of surrounding it (23). Single-sided designs allow the sensor to be smaller than it would otherwise have to be to accommodate large samples. Portable NMR sensors are also often nonimaging, they are designed to take quantitative NMR relaxometry measurements of a bulk sample rather than thin, slice-wise measurements. Nonimaging NMR sensors have long been used in oil well logging (24, 25), food quality control (26), and airport security (27). Single-sided sensors have more recently been used in quantifying properties of biological tissues such as skin, tendon, and breast tissue (23, 28).

Inspired by the broad success of NMR sensors operating at low magnetic field, we demonstrate that a portable, nonimaging, single-sided NMR sensor can rapidly assess clinically relevant changes in the fluid status of hypervolemic patients with ESRD and differentiate them from euvolemic healthy controls with stable volume status.

¹Harvard-MIT Division of Health Sciences and Technology (HST), Cambridge, MA 02139, USA. ²Koch Institute for Integrative Cancer Research, Massachusetts Institute of Technology, Cambridge, MA 02139, USA. ³Division of Nephrology, Department of Medicine, Massachusetts General Hospital, Boston, MA 02114, USA. ⁴A. A. Martinos Center for Biomedical Imaging, Massachusetts General Hospital, Boston, MA 02129, USA. ⁵Department of Physics, Harvard University, Cambridge, MA 02138, USA. ⁶Department of Materials Science and Engineering, Massachusetts Institute of Technology, Cambridge, MA 02139, USA.

*Corresponding author. Email: mjcima@mit.edu

We validate this finding by using quantitative MRI measurements and compare it to the performance of a U.S. Food and Drug Administration (FDA)-approved BI device.

RESULTS

Clinical study measuring participants at different fluid states

Seven patients with ESRD treated with chronic, thrice weekly HD and seven healthy control (HC) participants were enrolled into the study according to Institutional Review Board (IRB) guidelines, including written, informed consent. All enrolled HD participants were fluid overloaded, made apparent from clinical records of weight gain above their dry weight and the successful removal of fluid during their observed HD (used interchangeably in this text with dialysis) treatment. As is routine for dialysis treatments, ultrafiltration volume was informed by the change in weight from their target dry weight.

HD participants were measured before and after a single dialysis session, which allowed for a paired assessment of each participant at both a baseline state of hypervolemia and a later state closer to euvolemia after fluid removal. HC participants were subjected to the same clinical environment as HD participants: They sat in the same type of hospital bed for 4 hours, the length of a typical dialysis session, in the same hospital. It was assumed that HC participants would maintain a stable volume status throughout the study. Transverse proton NMR relaxation time (T_2) measurements were taken at the lower leg in all participants using both a 1.5-T MRI and a 0.28-T single-voxel, single-sided NMR sensor at the beginning and end of the study visit. BI measurements, weight, and blood draws were also taken at the same two time points (detailed in the “Study design” section of Materials and Methods). The demographics of the study cohort are summarized in Table 1, and participant-level data are detailed in table S1.

Tissue changes in response to dialysis by MRI

Quantitative T_2 MRI scans acquired at 1.5 T were used to determine which tissues and parameters (if any) changed in response to dialysis. Regions of interest (ROIs) were drawn in the MRI images to select distinct tissue groups (Fig. 1, A and B). The T_2 magnetization versus time $[M(t)]$ data of each pixel was fit to an exponential decay model determined by the extra sum-of-squares F test (table S2 and fig. S1). The optimal model was a biexponential decay for all tissues, except for bone, whose optimal model was monoexponential. The monoexponential model is a two-parameter fit, which produces an amplitude and relaxation time (A_{1-exp} , $T_{2,1-exp}$). The biexponential model is a four-parameter fit, which produces amplitudes and relaxation times for the short and long time components (A_{short} , $T_{2,short}$, A_{long} , $T_{2,long}$). The short component (A_{short} , $T_{2,short}$) of the biexponential fit of the muscle relates to intracellular fluid (ICF), whereas the long component (A_{long} , $T_{2,long}$) relates to extracellular fluid (ECF) (29–32)

$$M(t)_{1-exp} = A_{1-exp} e^{-\frac{t}{T_{2,1-exp}}}$$

$$M(t)_{2-exp} = A_{short} e^{-\frac{t}{T_{2,short}}} + A_{long} e^{-\frac{t}{T_{2,long}}}$$

T_2 relaxation time is a measure of the molecular environment of hydrogen atoms. A sample that is in a more liquid state (free fluids, ascites, and edema) has a longer relaxation time. A sample that has restricted mobility (cellular water bound to macromolecules) has a short relaxation time. Amplitude is a measure of the number of protons in a particular molecular environment. Relative amplitude (RA) measures the quantity of hydrogen atoms in a particular environment compared to the quantity of hydrogen atoms in all other measured environments. The RA of the long component,

Table 1. Demographics of study population. Hypervolemic patients with ESRD treated with hemodialysis (HD) and euvolemic healthy controls (HC) were recruited for the study. One HC participant and two HD participants completed the study twice. Reported blood value results are from baseline blood draws. Fluid loss (in kilograms) is based on the change between pre- and post-weight measurement. Percentage fluid loss is calculated by $100\% \times \text{fluid loss} / (0.6 \times \text{baseline weight})$, because about 60% of the body is water. Values represent mean \pm SD. NA, not applicable.

		Reference range	Healthy control (HC) participants	Hemodialysis (HD) participants
<i>n</i>	#		7 (6 unique)	7 (5 unique)
Age	years		54.2 \pm 4.9	55.1 \pm 10.3
% White			85.7%	42.9%
BMI	kg/m ²	18.5–24.9	25.1 \pm 4.4	27.8 \pm 5.0
Baseline weight	kg		75.4 \pm 12.2	82.8 \pm 16.1
Fluid loss	kg		0.6 \pm 0.2	2.2 \pm 1.2
Fluid loss	%		1.2 \pm 0.5	4.3 \pm 2.5
HD vintage	Days		NA	1013 \pm 699.8
Sodium	mM	134–144	140.6 \pm 2.1	139.1 \pm 1.6
BUN	mg/dl	6–24	16.0 \pm 4.4	58.1 \pm 14.5
Creatinine	mg/dl	0.76–1.27	0.8 \pm 0.2	8.3 \pm 1.8
WBC	$\times 10^3$ /ul	3.4–10.8	5.0 \pm 1.6	7.6 \pm 1.1
Platelets	$\times 10^3$ /ul	150–379	255.3 \pm 77.1	184.3 \pm 87.4
Osmolality	mOsm/kg	275–295	291.6 \pm 5.8	307.7 \pm 4.1
proBNP	pg/ml	<300	18.4 \pm 5.4	6086.1 \pm 4495.9

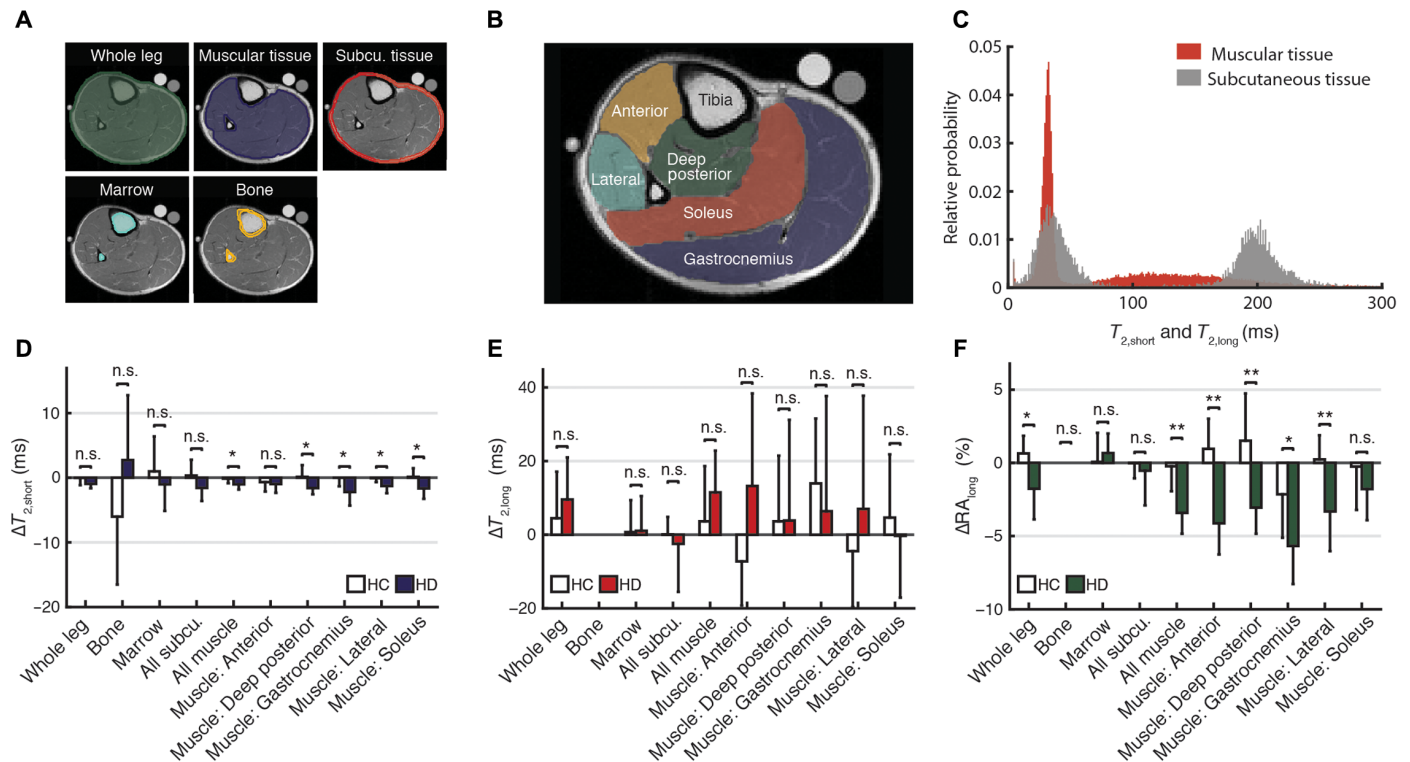


Fig. 1. MRI pixel-wise analysis of changes within ROIs. (A) The five ROIs—whole leg, muscular tissue, subcutaneous tissue, marrow and bone—that were drawn on each slice of each MRI scan. Subcutaneous tissue ROI includes skin, fat, and blood vessels in the fat. Muscular tissue ROI includes muscle, fascia, nerves, and blood vessels. (B) The muscle group ROIs—anterior, lateral, deep posterior, soleus, and gastrocnemius—that were drawn on the first slice of each scan. (C) A histogram of the pixel-wise short ($T_{2,short}$) and long ($T_{2,long}$) relaxation values found in the muscular and subcutaneous tissue of a representative participant. The pre-to-post change in (D) $T_{2,short}$, (E) $T_{2,long}$, and (F) RA_{long} for each ROI across all healthy control (HC, $n = 7$) and hemodialysis (HD, $n = 7$) participants. Bars represent the mean \pm SD. P values were calculated with a two-sample Welch test. For P values calculated with a two-sample Welch test, see table S3. n.s. denotes $P \geq 0.05$, * $P < 0.05$, ** $P < 0.01$.

RA_{long} (related to the relative amount of ECF), for example, is calculated by

$$RA_{long} = \frac{A_{long}}{A_{short} + A_{long}} \times 100\%$$

Figure 1C shows the pixel-wise $T_{2,short}$ and $T_{2,long}$ for muscle and subcutaneous tissue for a representative participant (fig. S2 shows this histogram for all participants). The $T_{2,short}$ values are similar in the two tissues, whereas the $T_{2,long}$ values differ with the subcutaneous compartment having the longer $T_{2,long}$. The change from pre- to post-measurement was calculated for each parameter ($T_{2,short}$, $T_{2,long}$, RA_{long}) in each tissue type (Fig. 1, D to F, corresponding statistics in table S3, and corresponding histograms in figs. S3 to S6). The muscle, muscle subgroups, and whole leg (which consists primarily of muscle) are the only tissues to display statistically significant changes, primarily in RA_{long} , in response to dialysis. RA_{long} changes by 1 to 7% across various tissues in the leg. It is possible to calculate the expected change in total body water (TBW) based on the amount of fluid removed from each participant, their baseline body weight, and the fact that the body is composed of about 60% water (6, 33). The amount of fluid removed is calculated on the basis of a participant's weight loss during the 4-hour period of dialysis/bed rest. Because the weight changes are acute, it is presumed that the reason for weight change is fluid loss rather than changes in body composition.

$$\text{Expected \% change in body water} = \frac{\text{fluid loss (kg)}}{0.6 * \text{baseline body weight (kg)}} \times 100\%$$

From this calculation, we expected to see $1.2 \pm 0.5\%$ (min, 0.8%; max, 2.2%) body water changes in HC participants and $4.3 \pm 2.6\%$ (min, 1.1%; max, 8.9%) body water changes in HD participants (Table 1 and table S1), which is consistent with the reported change in RA_{long} values in Fig. 1F. We did not expect the RA_{long} values to perfectly match because changes in ECF may not directly track TBW changes and certainly not in specific tissues.

MRI: T_2 relaxation times

The change in pixel-wise T_2 relaxation times was compared between HC and HD participants across each ROI (Fig. 1, D and E, and table S3). Although the change in the short relaxation time achieved statistical significance in some muscle groups, the size of these changes was small (<5 ms), which does not make it an ideal indicator and is of little diagnostic consequence because relaxation time measurements typically have a precision of a few milliseconds. Long relaxation times, $T_{2,long}$, did not have any statistically significant changes anywhere in the leg when comparing average HC and HD participant values.

Upon individual inspection, three participants were found to have quantifiably elevated $T_{2,long}$ values: HD1, HD1b, and HD2b. A cumulative distribution function (cdf) plot of $T_{2,long}$ in the whole leg shows that these three participants had relaxation times that were greater

than the 95% confidence interval of all participants (Fig. 2A). HD1, HD1b, and HD2b had among the highest concentrations of serum brain natriuretic peptide (BNP), a blood biomarker for volume overload (Fig. 2B). HD2b and HD1 had perifascial fluid deposits and subcutaneous edema visible on the MRI scans (although not detected on physical exam), which are precursors to pitting edema and can be seen in Fig. 2C as elevated relaxation time values bordering the leg.

MRI: Relative amplitudes

At baseline, most of the hypervolemic HD participants had elevated long RAs, RA_{long} , within the muscle compared to euvoletic HC participants (Fig. 2D and individual participant curves are plotted in fig. S7). An elevated RA_{long} value suggests that the ECF space of the tissue is expanded. The average RA_{long} for HD participants was significantly higher ($P < 0.01$) than that of HC participants at every percentile at baseline, which is expected because HD participants are hypervolemic and

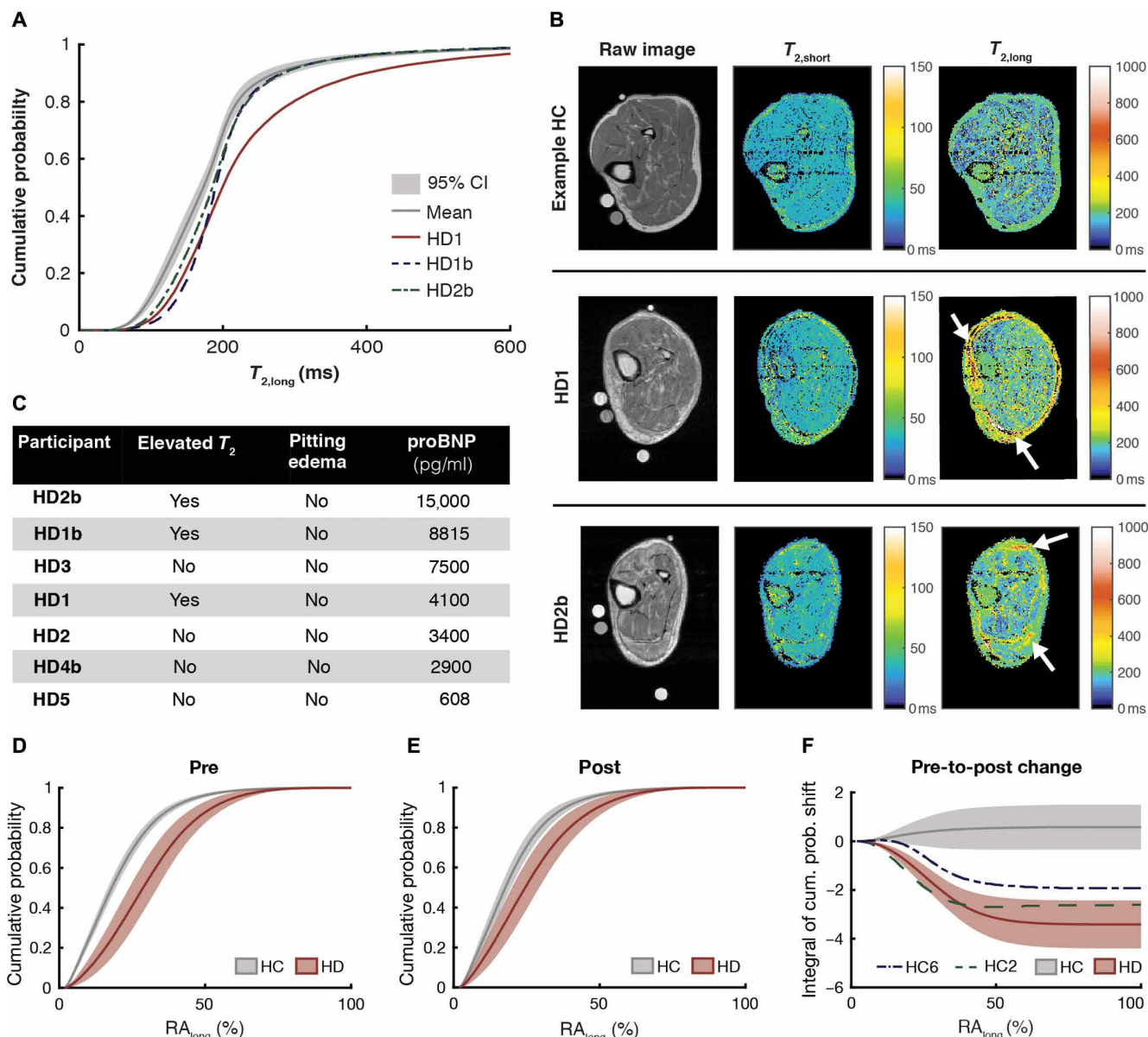


Fig. 2. MRI pixel-wise relaxation times and relative amplitudes. (A) Cumulative distribution function (CDF) of the pixel-wise $T_{2,long}$ values found within the entire leg at baseline. The mean and 95% confidence interval (CI) of all participants ($n = 14$) is in gray. HD1, HD1b, and HD2b relaxation times are shown separately. (B) Table summary of the proBNP and clinical examination results for HD participants ($n = 7$). The reference range for proBNP is < 300 pg/ml. (C) Heatmaps of $T_{2,short}$ and $T_{2,long}$ for a sample healthy control, HD1, and HD2b. Perifascial fluid deposits and/or subcutaneous edema are indicated by arrows. These fluid deposits and edema were not detectable on clinical exam. The average CDF of the pixel-wise RA_{long} values in the muscle of HC ($n = 7$) and HD ($n = 7$) participants at (D) pre- and (E) post-time points. (F) The change in RA_{long} for HC ($n = 5$ because HC2 and HC6 are plotted separately and not included in average) and HD ($n = 7$) participant groups. All CDF figures are plotted as mean \pm 95% confidence interval. Quantile regression P values corresponding to cdf plots are summarized in table S4. HC, healthy control; HD, hemodialysis. A "b" in the participant ID indicates a participant's second study visit for those that completed the study twice.

HC participants are euvoletic at baseline (table S4). The relative size of the ECF space, RA_{long} , of the muscle of HD participants decreased in response to dialysis such that their RA_{long} values were closer to those of euvoletic HC participants (Fig. 2, E and F, corresponding statistics in table S4). One of the main objectives of dialysis is to reduce excess ECF so that a patient reaches a euvoletic state (6).

The fitting of relaxivity data can also be performed on entire ROIs, which is a type of analysis similar to that of single-voxel NMR sensors rather than on individual pixels. Figure 3A shows the RA_{long} of the muscle ROI before and after dialysis; Fig. 3B shows the same data in boxplot form (participant-level data presented in table S5). The average muscle RA_{long} value for hypervolemic HD participants was 28.1%, whereas that of euvoletic HCs was 16.5%, with a statistically significant difference of $P = 0.0025$ between the groups (table S5). Figure 3C shows the change in RA_{long} before and after dialysis for the HD and HC groups. No significant change in RA_{long} occurred with HC participants ($P = 0.7499$), but the RA_{long} value for HD participants decreased by an average of 3.9% ($P = 0.0157$) (table S5). HC participants did not experience substantial changes in fluid status, whereas HD participants had a recorded volume of fluid removed.

These observations were statistically significant on the average; closer inspection at the individual participant-level data reveals some interesting detail. There were two HC participants—HC 2 and HC 6—that, similar to HD participants, experienced a decrease in RA_{long}

of the muscular tissue (Figs. 2F and 3A). We hypothesize that these two participants became dehydrated over the course of the study, as supported by their baseline blood values and subsequent intake and output (table S1). This hypothesis is consistent with our previous animal dehydration experiments, which showed the same pattern of RA decrease exclusively in the muscular tissue during acute dehydration (34). Furthermore, literature shows that nonexercise-based dehydration leads to a decrease primarily in the ECF of the muscle (35, 36).

Portable NMR sensor for bedside relaxometry measurements

Our laboratory has developed a nonimaging, single-sided, single-voxel NMR sensor that can be placed against most external soft-tissue parts of the anatomy (Fig. 4A; see additional sensor details in the “NMR sensor: Hardware” section of Materials and Methods) (37). The magnet has a 0.28-T main magnetic field (B_0) created by a unilateral Halbach magnet array (Fig. 4, B to E). The NMR sensor can collect 8000 data points along its T_2 decay curve measurement compared to only 32 points in the MRI measurement, which enables the NMR sensor data to be fit by a greater number of exponentials. Table S6 compares the specifications of a traditional MRI to those of our NMR sensor.

To understand how results from the two sensors compare to each other, we took back-to-back T_2 relaxation measurements of six phantom and ex vivo tissue samples with the same MRI, NMR sensor, and pulse sequences as in human measurements (fig. S8). The phantoms and ex vivo tissues spanned the T_2 relaxation time range that is found in the leg.

The NMR and MRI T_2 relaxation time measurements had a linear correlation of $r^2 = 0.966$ (Fig. 5 and raw values are plotted in fig. S9). The NMR sensor relaxation time measurements were within 10% and within 8 ms of the MRI measurements across all sample types except for the liquid copper sulfate measurement (table S7). The NMR sensor has a relatively nonuniform magnetic field compared to the MRI. T_2 measurements taken with a Carr-Purcell-Meiboom-Gill (CPMG) pulse sequence, as is our protocol, are affected by field gradient, interecho spacing, and the sample's diffusivity (24, 38). The larger any of these parameters, the greater the reduction of the measured T_2 relaxation time. The aqueous copper sulfate phantom has the largest diffusivity of any of the samples and therefore the worst correspondence between MRI and NMR sensor. Also, as expected, the aqueous copper sulfate's NMR sensor T_2 value is lower than its MRI T_2 value. The water diffusivities within tissues are not as large as those of liquid, with the exception of pockets of frank fluid accumulation. Therefore, good correspondence between our in vivo MRI and NMR sensor results was expected.

Bedside NMR measurements

We used the custom NMR sensor to take single-voxel T_2 measurements of the

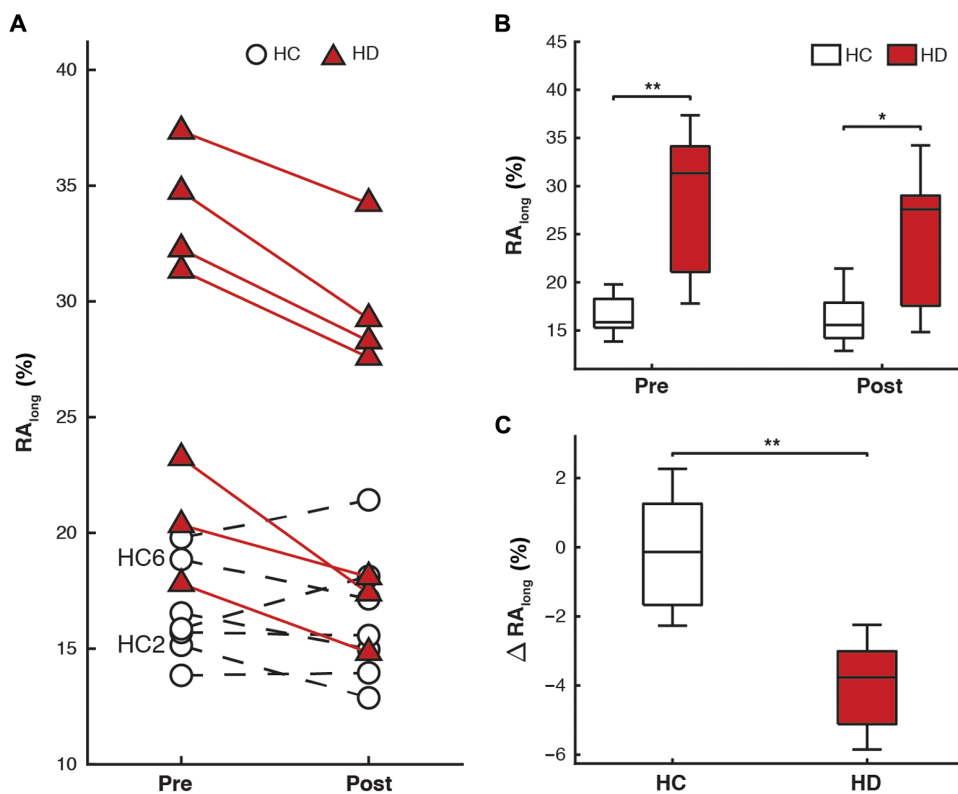


Fig. 3. MRI biexponential ROI results for the muscle. (A) The RA_{long} values of the muscle ROI for each participant ($n = 14$) before and after dialysis/bed rest. (B) Muscle RA_{long} values for HC ($n = 7$) and HD ($n = 7$) participants at pre- and post-time points. (C) The pre-to-post change in muscle RA_{long} for HC ($n = 7$) and HD ($n = 7$) participants. The central mark in each boxplot indicates the median, and the bottom and top edges of the box indicate the 25th and 75th percentiles, respectively. The whiskers that extend to the most extreme values were not considered outliers. P values were calculated using a two-sample permutation test. For P values calculated with a two-sample Welch test, see table S5. * $P < 0.05$, ** $P < 0.01$. HC, healthy control; HD, hemodialysis.

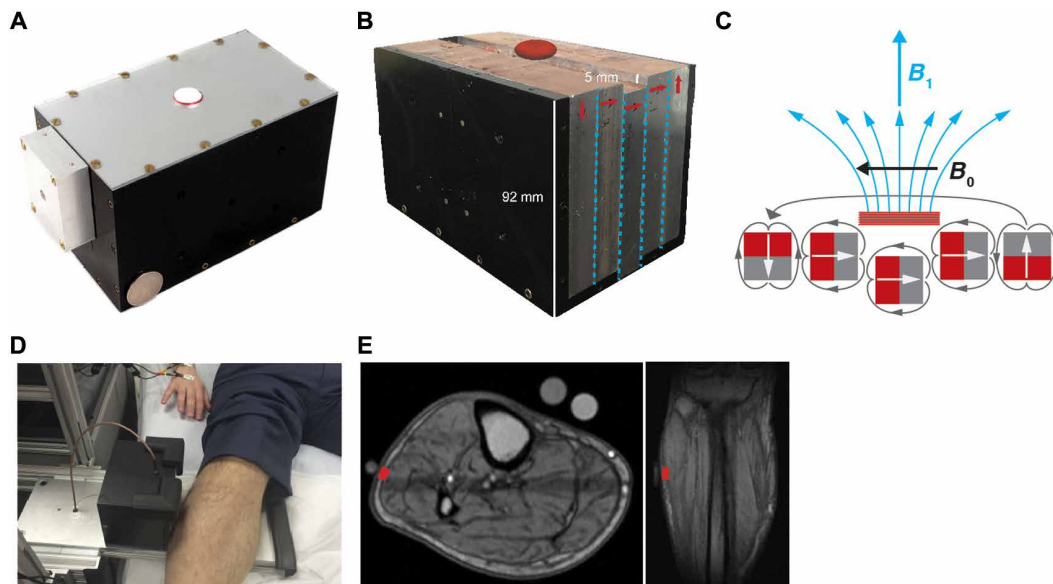


Fig. 4. Portable single-voxel NMR sensor for bedside relaxometry measurements. (A) Photo of the complete NMR sensor, RF coil, and side enclosure containing matching circuitry for the coil. A U.S. Quarter is shown for scale. (B) Photo of the NMR sensor with the top and side panels removed. The arrows denote magnetic orientation of each slab. The red ellipsoid above the sensor denotes approximate sensor measurement region. (C) Schematic of the linear Halbach design showing the orientations of the individual magnets as well as the net B_0 and B_1 fields. (D) Photo of the NMR sensor in use at the hospital for bedside assessment. The participant's leg is placed on top of the aluminum platform, which slides onto the bed. (E) Sagittal and transverse MRI scans showing the approximate location of the NMR sensor's measurement voxel in red.

same location (lateral aspect of lower leg; Fig. 4E) at the same time points as the MRI measurements. The NMR sensor's measurement voxel contained subcutaneous tissue and muscular tissue. The MRI pixel-wise results provided a model with which to analyze a voxel containing these tissues. Both subcutaneous and muscular tissues contain two components (a component is an amplitude and relaxation time pair) as determined by the F test. The short component, which corresponds to ICF, has a relaxation time $T_{2,short}$ that overlaps for both tissues. The long component, which relates to ECF, has a relaxation time $T_{2,long}$ that does not overlap between the muscle and subcutaneous tissue (Fig. 1C). A voxel containing both subcutaneous and muscular tissue, therefore, should consist of three distinct relaxation times. Advised by the anatomical model and measured correspondence between the relaxation times of the MRI and NMR sensor described above, these MRI results were used to develop a three-exponential model for the NMR sensor data

$$M(t)_{3exp} = A_a e^{-\frac{t}{T_{2,a}}} + A_b e^{-\frac{t}{T_{2,b}}} + A_c e^{-\frac{t}{T_{2,c}}}$$

where we define the relative magnitude of the relaxation times as $T_{2,a} < T_{2,b} < T_{2,c}$. Similarly, the RA of the second relaxation peak, $T_{2,b}$, is given by

$$RA_b = \frac{A_b}{A_a + A_b + A_c} \times 100\%$$

In the MRI pixel-wise results, the first exponential, $T_{2,a}$, was consistently observed near 40 ms (Fig. 1C). The third exponential was observed between 200 and 250 ms. We therefore fixed $T_{2,a}$ and $T_{2,c}$ in the NMR sensor's three-exponential model to values of 40 and 250 ms. The middle component ($T_{2,b}$, A_b), which was expected to correspond to ECF of the muscular tissue, was allowed to float. Thus, the fitted

parameters for each NMR sensor relaxivity measurement were $T_{2,b}$, A_a (RA_a), A_b (RA_b), A_c (RA_c). The amplitude of the middle component (RA_b) was expected to decrease in response to dialysis.

The MRI data shown in Fig. 1C suggest that the middle relaxation time should be about 70 to 170 ms. The middle relaxation time, $T_{2,b}$, of the NMR sensor data was fit to within the expected range (80 to 130 ms). No trends were observed in the relaxation time data of the NMR sensor. The NMR sensor's RA_b values, however, decreased significantly more in HD participants than in HC ones, just as was observed in the MRI data (Fig. 6A and table S8). This decrease corresponds to a reduction in the relative volume of ECF in the muscle. The relationship between the change in RA_b and change in ECF resistance, R_e , as measured by leg segmental BI is shown in Fig. 6B ($r^2 = 0.477$).

The baseline RA_b values were not statistically significantly different between HC and HD participants like they were when measured by MRI (Fig. 6C). This means that the NMR sensor cannot differentiate between euvoletic and fluid-overloaded participants using a single measurement. We hypothesize that the worse performance of the NMR sensor compared to MRI arises from the fact that the constant-volume NMR sensor voxel includes variable ratios of subcutaneous tissue to muscle tissue. That ratio will be constant when comparing the pre- and post-measurement for a given patient but will vary between patients. This may be the reason that we achieve significance between HD and HC groups for RA_b pre-to-post changes but not RA_b pre- or post-values by themselves for the NMR sensor. This hypothesis is supported the fact that the amplitude of the third component, RA_c (which corresponds to subcutaneous tissue), and the thickness of subcutaneous tissue for each patient were correlated ($r^2 = 0.67$; Fig. 6D). A greater subcutaneous tissue thickness means that subcutaneous tissue occupies a greater portion of the sensor voxel.

We explored the minimum voxel size and location that a future NMR sensor would have to measure to distinguish euvoletic from volume overload using a single measurement. We drew several small ROIs in multiple different locations on the lower leg MRI scans (Fig. 6E). The average T_2 decay curve of each ROI was analyzed with biexponential decay curves. The results of the small ROIs are summarized in Fig. 6F (tables S9 to S12). A 0.5-cm^3 voxel (1 cm by 1 cm by 0.5 cm) within the anterior ($P = 0.0198$) or lateral ($P = 0.0091$) muscle groups was calculated to be sufficient to detect fluid-overloaded participants with a single measurement. If the 0.5-cm^3 voxel was split between muscle and subcutaneous tissue, however, then the measurement could not distinguish between euvoletic HC and hypervolemic HD participants. More muscle tissue must be measured to distinguish fluid overload from euvoletic with a single measurement. These

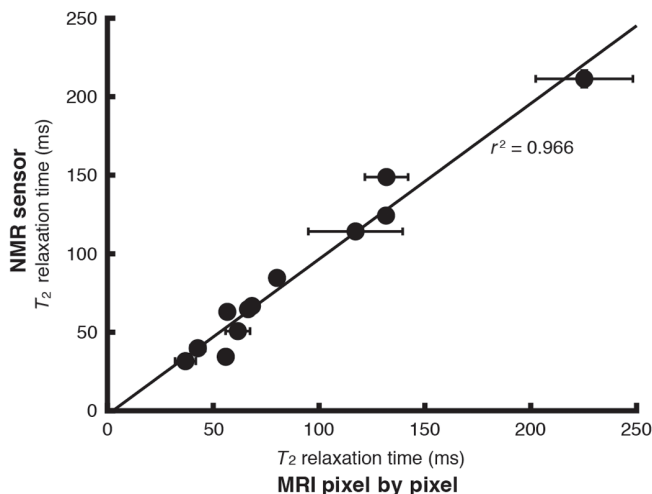


Fig. 5. Comparison of T_2 relaxation times measured by the NMR sensor and MRI. Scatter plot of fit results ($n = 6$ monoexponential and $n = 3$ biexponential fit results) for phantoms and ex vivo tissue samples measured on both the NMR sensor and MRI (pixel-by-pixel method). Correlation between the MRI and NMR sensor values is $r^2 = 0.966$. Vertical (NMR sensor) error bars represent the 95% confidence interval for the fit. Horizontal (MRI) error bars represent the SD of the pixel-by-pixel MRI results.

results provide a minimum volume, penetration depth, and anatomical measurement location to inform future NMR sensor designs. The methods for designing a sensor that can meet these volume and penetration depth requirements have been outlined by Bashyam *et al.* (37).

BI measurements

BI, like the NMR sensor, could not typically distinguish between hypervolemic HD and euvoletic HC participants using a single measurement. The results obtained with raw BI resistance values— R_e and R_{inf} —are summarized in Fig. 7 (A to H), and tables S13 to S16. Only the whole-body R_e measurement could distinguish the two populations using a single measurement at baseline ($R_{e, \text{whole body}}$; $P = 0.0201$). None of the leg BI measurements could do so. On the other hand, none of the whole-body BI measurements could distinguish between the change in volume status that accompanies dialysis treatments versus the stable volume status of HC participants. Both segmental leg measurements could do so ($\Delta R_{e, \text{leg}}$; $P = 0.0383$, $\Delta R_{inf, \text{leg}}$; $P = 0.0023$). The ECF and TBW volumes obtained by inserting the raw BI resistance values into predictive equations are summarized in Fig. 7 (I to P). BI could not statistically significantly distinguish between euvoletic HC and hypervolemic HD participants when volume equations were applied across most measurement types, except for the $\Delta ECF_{\text{whole-body}}$ measurement ($\Delta ECF_{\text{whole-body}}$; $P = 0.027$).

DISCUSSION

Quantitative relaxometry—through both traditional MRI and non-imaging NMR sensors—can provide data about a patient's fluid status. Recruiting HD participants allowed us to study a hypervolemic population that became less hypervolemic at the end of the study, thereby allowing for paired analyses of the same person at two distinct fluid levels. HC participants were assumed to remain euvoletic throughout the study, although a few unexpected cases of dehydration were en-

countered. Even with our small sample size, we were able to differentiate between participants who were euvoletic or had varying degrees of volume overload (fig. S10). In addition, the MRI results seemed sensitive to participants who showed evidence of dehydration. None of the participants displayed clinical signs of volume overload on physical exam. Relaxometry metrics may be able to detect fluid overload before traditional clinical examination, which is the principle test used by physicians today.

The first sign of fluid overload in the lower leg region among the patients studied was an elevation in the RA_{long} in the muscle, which indicates an expanded relative ratio of ECF. Hypervolemic HD participants could be distinguished from euvoletic HC participants using a single MRI measurement of RA_{long} captured at a single time point. The two populations could also be distinguished via the MRI or NMR sensor's measurement of change in muscle RA_{long} and RA_b , respectively, which are related to a decrease in the relative ratio of muscle ECF. The observed changes in RA_{long} and RA_b values are within the expected range based on the percentage of fluid loss from study participants. An exploration of voxel sizes revealed that if a future NMR sensor can measure 0.5 cm^3 of the lateral or anterior lower leg muscles, then it should be able to distinguish euvoletic HC from hypervolemic HD participants based on a single measurement as well.

The $T_{2, \text{long}}$ of the lower leg among our most volume-overloaded patients was elevated, indicating that the molecular environment of the ECF space of these participants became more aqueous than normal. Previously published studies involving patients who were more volume overloaded than our patient population reported relaxation time increases in the lower leg as well (39, 40). To our knowledge, no studies have reported the RA_{long} increase that precedes relaxation time elevation.

We interpret these relaxometry findings with consideration of the physiologic mechanisms in place to regulate the distribution of salt and water. In the absence of kidney function (ESRD), nearly all salt and water intake is retained (save for small amounts lost via gastrointestinal and insensible excretion), which leads to expansion of the vascular space (41). The muscle's rich microvasculature network causes an initial predominance of interstitial fluid accumulation in the muscle as opposed to less vascular tissues. Eventually, the capacity of the muscle to hold excess water is exceeded, and lymphatic drainage is necessary. Lymphatic reabsorption occurs primarily in the subcutaneous tissue space, which is why per fascial fluid and subcutaneous edema are seen in more advanced cases of fluid overload (40). The removal of fluid via the vascular space, as in HD, leads to fluid removal in the same order as accumulation occurred, with well-vascularized muscle responding first.

One of the main objectives of HD is to reduce excess ECF volume (1, 5, 17, 22). Thus, the extent and location where those decreases occur can be quantified with MRI or, more economically, with a portable NMR sensor assuming that ECF volume scales with RA_{long} and RA_b , respectively. The observation that the RA_{long} of HD participants in the postdialysis measurement approaches the RA_{long} of HC participants matches the clinical observation that well-tolerated intradialytic fluid removal brings a hypervolemic patient closer to euvoletic status. We can speculate that the RA_{long} of HC participants represents something of a reference range for euvoletic, but further study is needed to explore this as a potential criterion for NMR-driven fluid removal during dialysis.

Furthermore, the amount of baseline hypervolemia typically encountered in maintenance HD patients represents the level of fluid overload for which it is most critical to have accurate clinical sensors.

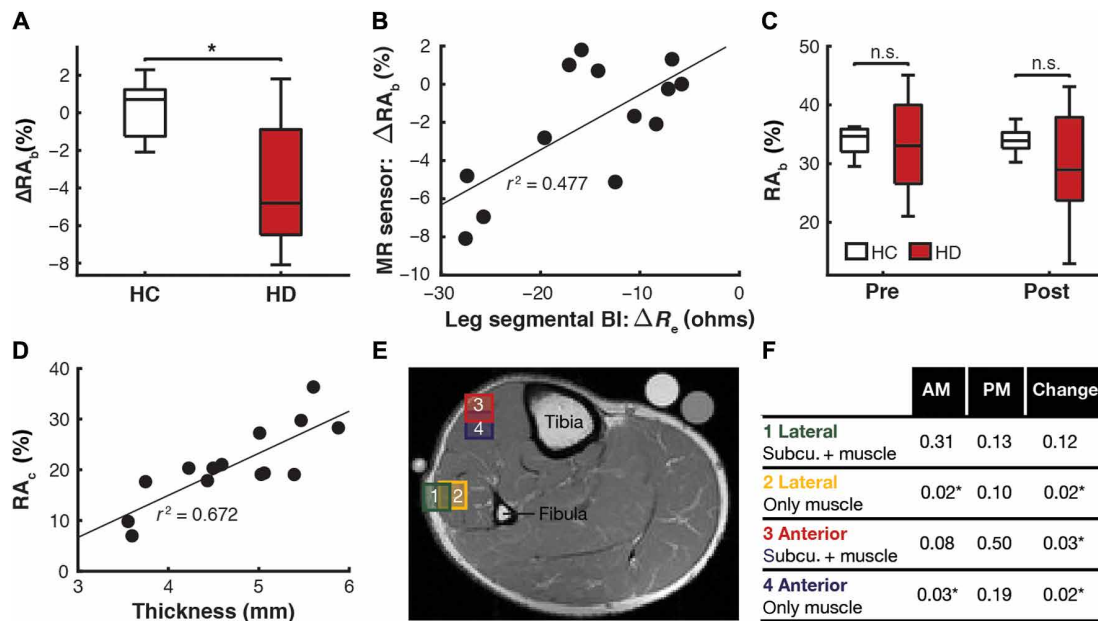


Fig. 6. NMR sensor results and future sensor design criteria. (A) Boxplots displaying the pre-to-post change in NMR sensor's RA_b values for HC ($n = 7$) and HD ($n = 7$) participants. (B) Change in RA_b values plotted the change in ECF-associated resistance, $R_{e, leg}$ ($r^2 = 0.477$) ($n = 13$ because BI sensor malfunctioned during HC6 post measurement). (C) Boxplots displaying the NMR sensor's RA_b values at pre- and post-time points for HC ($n = 7$) and HD ($n = 7$) participants. The central mark in each box plot indicates the median, and the bottom and top edges of the box indicate the 25th and 75th percentiles, respectively. The whiskers that extend to the most extreme values were not considered outliers. P values for (A) and (C) were calculated using a two-sample permutation test. For P values calculated with a two-sample Welch test, see table S8. (D) NMR sensor's RA_c plotted against subcutaneous tissue thickness ($r^2 = 0.672$, $n = 14$). The tissue thickness gets compressed by a few millimeters when the leg is pressed against the NMR sensor's hard surface during measurement. (E) MRI scan (transverse cross section of the calf) showing the size and location of the four smaller MRI ROIs that were analyzed. (F) Summary of P values showing the ability of the smaller ROIs [in (C)] to distinguish between euvoletic HC ($n = 7$) and hypervolemic HD ($n = 7$) participants. P values were calculated using a two-sample permutation test. For P values calculated with a two-sample Welch test, see tables S9 to S12. * $P < 0.05$. HC, healthy control; HD, hemodialysis.

Clinicians do not need a sensor to determine that a patient with pitting edema, for example, is fluid overloaded. Clinicians would benefit, however, from a sensor that can detect the type of lower-level hypervolemia (<5 liters) in patients receiving chronic HD. Physical signs are typically not visible at this stage of hypervolemia, yet this level of fluid accumulation is nevertheless associated with increased morbidity and mortality (3, 6, 42).

HD consists of both ultrafiltration and removal of waste. We expect filtration to affect the relaxation times rather than the RAs because relaxation time is a measure of molecular environment. Furthermore, urea—a compound that accumulates in the body of patients with ESRD—is a known T_2 -shortening agent that diffuses through all fluid spaces in the body (43, 44). If levels of urea were affecting our relaxometry measurements, then we would expect the T_2 relaxation times to be lower in HD participants than in HCs and then to increase after dialysis. In reality, T_2 relaxation times of HD participants were equal to or higher than those of HCs at all time points. Future studies will aim to fully decipher the role of these two processes by measuring HD patients that have pure filtration or pure fluid removal functions performed on them during dialysis, as well as by measuring nonuremic fluid-overloaded participants, such as patients with congestive heart failure with preserved renal function.

Our findings suggest that bedside NMR measurements may be a safe, noninvasive method to identify fluid overload and, therefore, inform therapy in patients with ESRD (guide dry weight determination) and potentially other patient populations (titrate diuretics in heart failure) to attain euvoemia with greater clinical efficacy. NMR

has many benefits over other fluid-monitoring modalities. Continuous blood volume monitoring measures only relative blood volume changes, which can help reduce hypotensive episodes during dialysis but cannot tell whether a participant has attained their true dry weight or has residual fluid overload (5, 6, 17). BI is affected by factors like sweat, electrode placement, body shape assumptions, and the validity of population-specific equations, whereas NMR intrinsically measures signal from water molecules (5, 17, 45). In our head-to-head comparison of BI to magnetic resonance, BI measurements generally performed worse than MRI and comparably to the NMR sensor. The body resistance measured by a low-frequency current from wrist-to-ankle electrodes— $R_{e, whole body}$ —was the only BI measurement that was able to statistically significantly distinguish between the HC and HD groups using a single baseline measurement. Ironically, however, the statistical significance was lost when the raw R_e resistance values were inserted into an FDA-approved equation to estimate ECF volume in terms of liters. The BI device used is FDA-approved for estimating whole-body composition—including TBW and ECF—for healthy individuals with normal fluid physiologies. The loss of significance when converting from R_e to ECF volume likely comes from inserting data from dialysis patients into algorithms developed on euvoletic, healthy participants. The benefit of NMR over BI is that it inherently measures fluid volume (a benefit that is harnessed by the oil and food quality control industries) without relying on population-specific equations and assumptions about body shape.

One of the limitations of this study is that there were only 14 participants (7 in each group) due to the burden that the study design

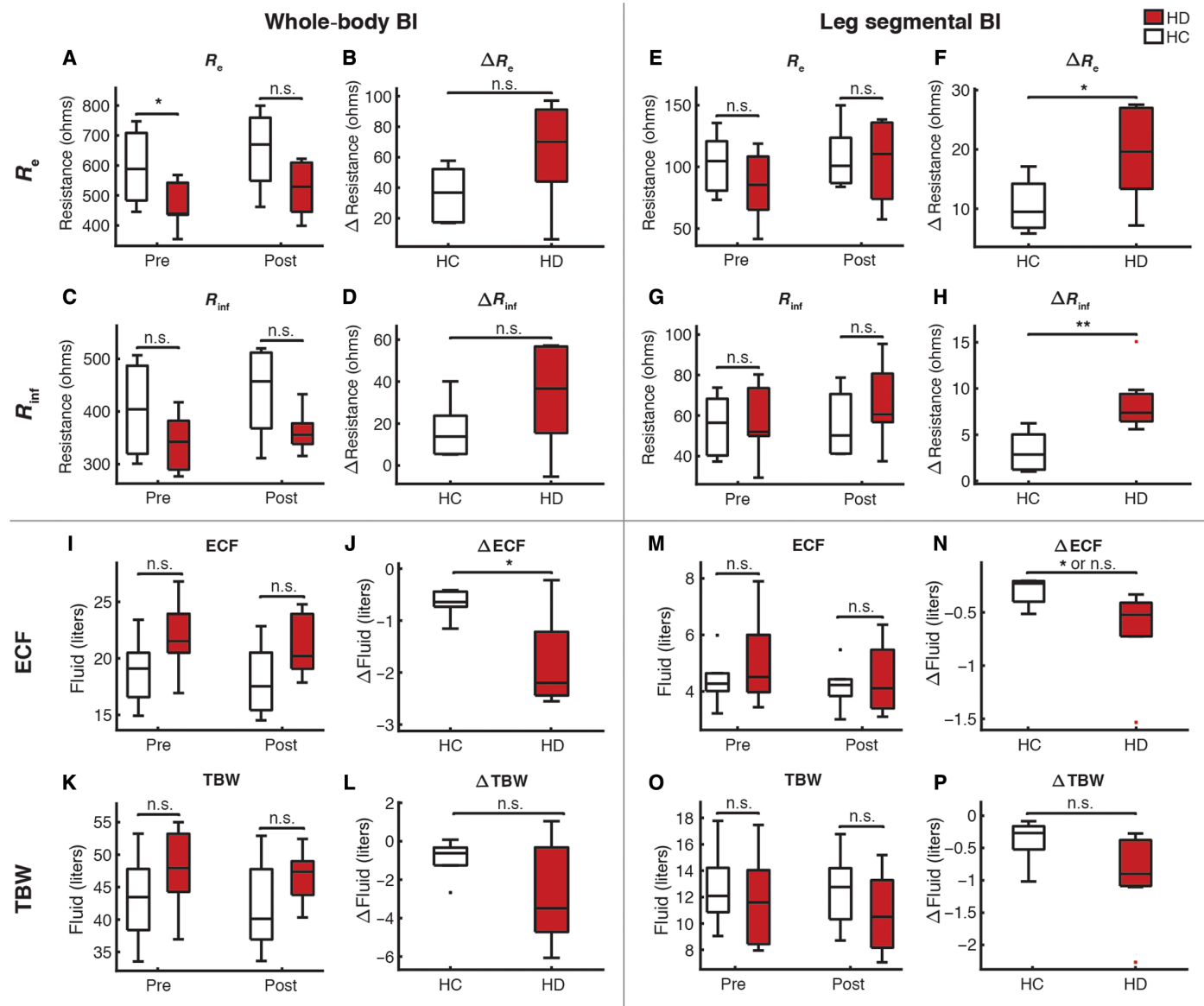


Fig. 7. Whole-body and leg BI results. (A to H) Top two quadrants: Raw BI resistance measurements (R_e and R_{inf}). (I to P) Bottom two quadrants: Volume measurements (ECF and TBW) ($n = 7$ HC, $n = 7$ HD). (A) to (D) and (I) to (L) (the two left quadrants) come from whole-body BI measurements, whereas (E) to (H) and (M) to (P) (the two right quadrants) come from leg segmental BI measurements. The top row of panels within each quadrant shows R_e /ECF data. The bottom row of panels within each quadrant shows R_{inf} /TBW data. Low in vivo resistance measurements indicate that more fluid is present in the body. Higher resistance measurements indicate that less fluid is present. An increase in resistance indicates a decrease of fluid. Statistics were calculated with both a two-sample Welch test and two-sample permutation test for all plots. The significance level was the same for both statistical tests across all plots except for subplot (N), where the permutation test was significant ($P = 0.014$) but Welch test was not ($P = 0.054$). P values for (A) to (H) are summarized in tables S13 to S16. The P value for (J) is $P = 0.027$. n.s. indicates $P > 0.05$, * $P < 0.05$, ** $P < 0.01$. HC, healthy control; HD, hemodialysis.

placed on dialysis patients, who are chronically ill. The HD participants had to travel to the study site, rather than their local dialysis unit, and booked their dialysis treatment with an additional hour of imaging. We chose to obtain pre- and postdialysis measurements from each participant so that each participant could serve as his own control in an effort to mitigate the limited number of participants in the study. Another limitation is the fact that there may be other aspects of physiology (uremia and overall health) that make HC and HD

participants different from one another other than simple fluid status. Larger future studies should expand to other patient populations to address these confounders.

The proof-of-concept in vivo NMR sensing for fluid status shown here is only one of the many possible uses for point-of-care relaxometry. Many diagnostic use cases for quantitative NMR biomarkers already exist, such as monitoring progression of multiple sclerosis, assessing iron overload in the liver, and identifying inflammatory

muscular disorders (46–48). Portable NMR sensors can make it economically feasible to bring these new diagnostic discoveries to the clinic and improve patient care.

Future NMR sensor designs are not limited to a single-sided design or even to permanent magnets. Future work should experiment with lower field strengths, different purpose-built magnet constructions (optimized for curved surfaces or greater penetration depths), and other parts of the anatomy (lung and abdomen) (49–53). The measurement of additional relaxometry parameters, like T_1 , or taking two-dimensional measurements such as T_2 -diffusion or T_1 - T_2 , will enable further probing into physiology. The results of this study lay the groundwork for the diagnostic potential of NMR measurements to be brought out of radiology suites to the patient bedside and, eventually, into the patient's home.

MATERIALS AND METHODS

Study design

The overall goal of the work was to study the relaxometry findings that accompany changes in fluid status using both a portable NMR sensor and traditional MRI. For each participant, contact began and ended with MRI scans and consisted of HD (for HD participants) or bed rest (for HC participants) in between the two scans. MRI scans were conducted at the Athinoula A. Martinos Center for Biomedical Imaging (Charlestown, MA) and dialysis/bed rest was conducted at the Massachusetts General Hospital (MGH) Main Campus (Boston, MA) in either the Dialysis Unit or the Clinical Research Center.

HD participants received their usual HD treatment (3 to 4 hours) in a hospital bed (in a reclined supine position with legs outstretched). HC participants sat on the same type of hospital bed for 4 hours. All intake and output were recorded for each participant during this interval. The following set of measurements was taken at the start and end of the dialysis/bed rest period:

- 1) Standing weight measurement
- 2) Blood work
- 3) Portable NMR sensor measurements: T_2 measurements of the lower leg with the single-sided NMR sensor
- 4) BI measurements: whole-body (wrist-to-ankle electrode placement) and leg segmental (upper calf-to-lower calf electrode placement) measurements

Protocols for each measurement are detailed in subsequent sections. All participants were given the option of a to-go snack before returning to the Martinos Center for the second MRI.

Patient population

Seven patients with ESRD maintained with chronic thrice weekly HD and seven HC participants were recruited. One HC participant and two HD participants completed the study twice (denoted by “b” in the participant ID of their second visit). Participants were recruited from the Partners HealthCare clinical study recruitment email list, from recommendations from nephrologists, or from previous participation in pilot studies (when agreed to be contacted again). Enrollment was limited to males over the age of 25 years with a body mass index (BMI) between 18.5 and 40. Patients were excluded if they had a pacemaker, metal implants, or severe anemia (Hgb < 7.5 mg/dl) or had a history of limb amputation. HC participants reported no history of renal disease, cardiac disease, or other chronic conditions. HD and HC participants were age-matched by decade. Basic demographics were recorded for all participants. The study was approved by the

Partners Human Research Committee, which is Partners HealthCare's IRB (Partners approval no. 2015P000011), and written, informed consent was obtained from each participant.

Blood work

All participants had blood drawn at the beginning of the 4-hour study interval after the first MRI. Laboratory work included the following: serum sodium, blood urea nitrogen (BUN), creatinine, complete hemoglobin and hematocrit, serum osmolality, and B-type natriuretic peptide (proBNP). HD participants also had routine pre- and post-dialysis laboratories as dictated by our hospital's dialysis unit protocols, and a sample of blood was collected for storage in a biorepository.

MRI scans

MRI scans of the lower leg (upper calf) were obtained on a 1.5-T Siemens Avanto Scanner (Siemens Medical Solutions, software version Syngo MR B17) and CP extremity coil at the Martinos Center (Charlestown, MA). The upper calf (right leg for HC participants; leg contralateral to dialysis access site for HD participants) was positioned at the center of the extremity coil using padding when necessary. A localizing capsule was placed on the lateral aspect of the widest part of the calf (MR-SPOT 121, Beekley Medical Corp.). An initial set of localizing MRI scans were performed to find the location of the capsule [scanning sequence/variant, GR/SP (fl2d1); repetition time TR = 7.7 ms; echo time TE = 3.28 ms; flip angle FA = 20°; slice thickness = 6 mm; three slices in each anatomical direction]. A quantitative multiecho spin echo T_2 scan (se2d32) was performed with parameters TR = 3300 ms, TE = 8 ms, 32 echoes, 1 average, 4 sagittal slices of 5-mm thickness with 60% spacing (3 mm) between slices, 192 × 144 matrix (75% phase field of view), 1 × 1-mm in-plane pixel resolution, and a total acquisition time of 7 min 53 s. The sagittal scans were positioned such that the localizing capsule appeared in every slice.

MRI analysis: Software

The raw digital imaging and communications in medicine (DICOM) images from the scanner were converted to Neuroimaging Informatics Technology Initiative (NIfTI) format with FreeSurfer software (Martinos Center, Charlestown, MA), ROIs were hand-drawn on each slice of each scan using FSleyes (previously FSLview) (54), and all further analyses were performed in MATLAB 2017b (MathWorks Inc., Natick, MA). All processing scripts are available in the repository: <https://github.com/lcolucci/portable-nmr>.

The hand-drawn ROIs were as follows: (i) Subcutaneous tissue: includes skin, fat and blood vessels in the fat; (ii) Bone and marrow: both include tibia and fibula; (iii) Muscular tissue: includes muscle, fascia, nerves, and blood vessels; and (iv) Whole leg: includes all of the aforementioned tissues. The following muscle group ROIs were drawn on the first slice of each scan: gastrocnemius (includes both medial and lateral heads), soleus, deep posterior (includes flexor hallucis longus, tibialis posterior, and flexor digitorum longus), anterior (includes tibialis anterior, extensor hallucis longus, and extensor digitorum longus), and lateral (includes peroneus brevis and peroneus longus).

MRI analysis: Pixel-wise

The quantitative T_2 MRI images were analyzed by fitting each pixel on each slice with a mono- and biexponential decay. An F test was used to determine the optimal model for pixels within each tissue type (table S2), which showed that a biexponential fit was optimal for all tissue types except for bone. The initial point of the T_2 decay

was ignored because of lack of stimulated echo effects. There were a total of 31 points from 16 to 256 ms with 8 ms of spacing that were fit to the following equations

$$M(t)_{1\text{-exp}} = A_{1\text{-exp}} e^{-\frac{t}{T_{2,1\text{-exp}}}}$$

$$M(t)_{2\text{-exp}} = A_{\text{short}} e^{-\frac{t}{T_{2,\text{short}}}} + A_{\text{long}} e^{-\frac{t}{T_{2,\text{long}}}}$$

The starting values used for the biexponential fit were ($A_{\text{short}} = 1500$, $T_{2,\text{short}} = 50$, $A_{\text{long}} = 1500$, $T_{2,\text{long}} = 210$). The upper and lower limits for the fittings were set to 10,000 and 0, respectively. A non-linear least-squares fitting method with a trust-region algorithm was used to perform the fits using MATLAB 2017b.

Pixel fit results were deleted if any of the following criteria were met: (i) the root mean squared error (RMSE) of the pixel fit was greater than the 99th RMSE percentile for that scan, (ii) either of the two relaxation times was less than $0.5 \text{ TE} = 4 \text{ ms}$, (iii) either of the two relaxation times was greater than the maximum T_2 that could be expected to be measured with less than 5% relative error [calculated by the empirically derived expression $25.63 * \text{signal-to-noise ratio (SNR)} + 197.6$], (iv) the 95% confidence interval of any parameter was fit to NaN, or (v) the difference between the two relaxation times was less than 10 ms. Figure S26 shows all pixels that were deleted because of these criteria.

The cdf plots of the pixel-wise data visually show the percentage of pixels that are below a particular value (for code, see the “Computer code for statistical tests: no. 5 cdf plots for pixel-wise MRI data” section of the Supplementary Materials; fig. S7) The pre-to-post change for pixel-wise data is calculated by first subtracting the pre- and post-cdfs from each other and then integrating across the difference cdf curve (Fig. 2F).

MRI analysis: ROI

All pixels within an ROI were averaged together to produce a single T_2 decay curve. A mono- or biexponential fit was then performed on the average 31-point (because the first point was ignored) decay for that ROI according to the same specifications described in the pixel-wise section above.

Subcutaneous thickness measurements

The subcutaneous tissue thicknesses for each participant were calculated from the MRI-localizing scans using the length measurement tool on the software program OsiriX Lite DICOM Viewer (Pixmeo SARL). The thickness of the subcutaneous tissue was measured in four locations around the localizing marker on each of the three sagittal localizer slices for both pre- and post-scans. All 24 subcutaneous thickness values were averaged together to obtain the average skin and subcutaneous thickness for a particular participant. The subcutaneous tissue thickness traversed by the NMR sensor is less than the values measured with this method. The subcutaneous tissue is compressed by a few millimeters during data collection when the leg is pressed against the hard surface of the NMR sensor.

NMR sensor: Clinical setup

The NMR sensor was attached to the platform of a custom aluminum cart that extended onto the patient’s bed (Fig. 4D). The participant’s pant leg was rolled up, and their lower leg was put directly on the aluminum platform for electrical grounding and directly

against the surface of the sensor coil (Fig. 4D). The cart position was adjusted such that the sensor coil was on the same spot as the MRI-localizing marker. This ensured that the NMR sensor measured the same anatomical location as the MRI. Participants were instructed not to move their leg for the duration of the NMR measurement, and data collection was restarted if patients moved.

Ambient and magnet temperatures were recorded throughout the dialysis session with a continuous temperature logger and K-type thermocouples (RDXL4SD, OMEGA Engineering). A phantom filled with an aqueous solution of copper sulfate of known T_2 relaxation time was taken with each human measurement so that any sensor malfunctions could be immediately identified. Ambient temperatures tended to rise throughout the study because of the body heat of the study participant and study staff sitting in a small hospital room. The measured T_2 of the phantom, however, did not change by more than 2.8 ms (an outlier that occurred once). The average pre-to-post change in measured phantom T_2 value was, in fact, much smaller at $0.84 \pm 0.78 \text{ ms}$ (table S17). This phantom validation step ensured that the sensor was functioning properly and measured consistent T_2 values throughout the study.

NMR sensor: Hardware

We developed a custom single-sided, sweet-spot NMR sensor for this study that can be placed against most external soft-tissue parts of the body. The magnet has a 0.28-T main magnetic field (B_0) created by a unilateral linear Halbach design (37). The magnetic field is created by 180 cuboidal neodymium iron boron (NdFeB, N52 grade) magnets (Viona Magnetics, New York, USA) positioned across five slabs in a 6×6 grid within each slab. Each magnet’s magnetization orientation points in a different direction based on which slab it is in, as shown in Fig. 4, B and C. The sensor weighs about 4.9 kg and measures about 9 cm by 9 cm by 15 cm.

Our magnet’s “sweet spot” region has a saddle shape where the B_0 field is about 80 mm^3 (4 mm by 5 mm by 4 mm) in volume at 0.28-T field strength (B_0 field map shown in fig. S12). The transmit-receive coil is a single circular solenoid coil about 1.6 cm in diameter tuned to 11.61 MHz. More about the sensor design can be read by Bashyam *et al.* (37). The custom magnet was connected to a Kea2 spectrometer with dual transmit channels at 1 to 100 MHz and a duplexer/preamplifier module operating from 7 to 16 MHz (Magritek, Ltd., Wellington, New Zealand and Aachen, Germany).

NMR sensor: Pulse sequences

Prospa software was used to run various pulse sequences (Magritek, Ltd., Wellington, New Zealand and Aachen, Germany). The T_2 measurements were taken using a CPMG pulse sequence with 8000 echoes, 65- μs echo time, 3 dummy echoes, 12- μs pulse length, 16 points per echo, 0.5- μs dwell time, 2000-kHz bandwidth, 800- to 3500-ms inter-experimental delay, autophasing, 8 averages per measurement, and 11.61-Mz B_1 frequency. Hard 90° and 180° pulses were used (-12 - and -6 -dB pulse attenuation, respectively), and phase cycling was performed. Eight averages were taken per measurement, and 3 to 10 measurements per time point were averaged together in the post-processing analysis.

NMR sensor: Data analysis

The T_2 decays from each time point were averaged together using a straight-averaging technique. The first point was deleted from the averaged decay. The averaged decay is plotted in fig. S13 for a representative

HC and HD participant. The average SNR of all participants across all time points is 80.4 ± 24.5 (mean \pm SD). SNR was calculated as the ratio of the maximum value of T_2 decay curve divided by the SD of the noise floor at the end of the T_2 decay. The decay signal was fit to a three-exponential decay on the basis of the model developed through the MRI pixel-by-pixel results. The NMR sensor data were forced to fit to a three-exponential decay where the first exponential was fixed at 40 ms, the third exponential was fixed at 250 ms, and all other parameters were allowed to float.

$$M(t)_{3\text{-exp}} = A_a e^{-\frac{t}{40 \text{ ms}}} + A_b e^{-\frac{t}{T_{2b}}} + A_c e^{-\frac{t}{250 \text{ ms}}}$$

The starting values used for the fit were ($A_a = 9$, $A_b = 5$, $A_c = 7$, $T_{2b} = 100$). The lower and upper limits for the fittings were set to zero and infinity, respectively, for the amplitudes, and 0 and 250 for relaxation time 2. A nonlinear least-squares fitting method with a trust-region algorithm was used to perform the fits using MATLAB 2017b (MathWorks Inc., Natick, MA).

Phantoms and ex vivo tissues

Three phantoms—vegetable oil, agar, and an aqueous copper sulfate solution (CuSO_4 ; Sigma-Aldrich, Missouri, USA)—and three ex vivo tissue samples—muscle (bovine), fat (porcine), and skin (porcine)—were measured with the MRI and NMR sensor protocols described above for human participants. The aqueous copper sulfate was diluted with deionized water to ensure a longer relaxation time. The ex vivo tissues were kept in a sealed petri dish to avoid dehydration over time. The agar-based phantom was made by the protocol in Hattori *et al.* (55).

BI: Setup

BI spectroscopy measurements were taken with an ImpediMed SFB7 unit and dual-tab body composition electrodes (ImpediMed, Ltd., Australia). The system uses a single-channel tetrapolar configuration and performs a frequency sweep of 256 frequencies from 10 to 500 kHz. The ImpediMed Bioimp software (version 5.4.0.3) was used to apply Cole analysis and Hanai mixture theory to the raw data. For whole-body BI measurements, the two dual-tab electrodes were placed at the wrist and ankle of the side of the body contralateral to the dialysis patient's access (right side for HCs). For the leg segmental BI measurements, the two dual-tab electrodes were placed at the lateral aspect of the lower leg at the same side of the body. The distance between the two leg electrodes and the lower leg length (from fibula head to the lateral malleolus) was recorded.

BI: Analysis

Three BI measurements were taken at the pre- and post-time points, and results were averaged together. If any of the resistance values fit by the model were zero, then the trial was excluded from the average. The R_e (modeled zero-frequency resistance, correlated to ECF), R_{inf} (modeled infinite-frequency resistance, correlated to TBW), and whole-body TBW and ECF values were taken directly from the ImpediMed Bioimp software (FDA-approved for healthy, euvoletic individuals). The leg segmental TBW and ECF values were manually calculated on the basis of the following equations published in the Hydra Model 4200 Manual (56)

$$\text{ECF} = \frac{\rho_{\text{ECF}}^{2/3}}{3 * (4\pi)^{1/3} * 1000} * L * (C_1^2 + C_2^2 + C_1 C_2) * \left(\frac{L}{C_1 C_2 R_E} \right)^{2/3}$$

$$\left(1 + \frac{\text{ICF}}{\text{ECF}} \right)^{5/2} = \left(\frac{R_e + R_i}{R_i} \right) \left(1 + \frac{k_p \text{ICF}}{\text{ECF}} \right)$$

$$k_p = \frac{\rho_{\text{ICF}}}{\rho_{\text{ECF}}}$$

$$\text{TBW} = \text{ECF} + \text{ICF}$$

where ECF is the predicted segmental extracellular fluid volume (liter), ICF is the predicted segmental intracellular fluid volume (liter), ρ_{ECF} is the resistivity of the extracellular fluid (ohms·m) [273.9 ohms·m for males and 235.5 ohms·m for females (values provided by ImpediMed Inc.)], ρ_{ICF} is the resistivity of the intracellular fluid (ohms·m) [937.2 ohms·m for males and 894.2 ohms·m for females (values provided by ImpediMed Inc.)], L is the lower leg length (cm), C_1 is the lower leg circumference (cm), C_2 is the lower leg circumference (cm), R_e is the extracellular resistance value from the model fitting (ohms), and R_i is the intracellular resistance value from the model fitting (ohms).

The reported $\text{ECF}_{\text{leg segmental}}$ and $\text{TBW}_{\text{leg segmental}}$ values were calculated using lower leg length, rather than electrode spacing because electrode spacing was not recorded for participant HC3.

Statistical analyses

Statistical tests were calculated in MATLAB 2017b (MathWorks Inc., Natick, MA) and RStudio (RStudio Inc., Boston, MA). All tests were two sided, and $P < 0.05$ was considered statistically significant. All statistics presented in this paper fall into one of the following four categories. The MATLAB or R commands corresponding to each of these statistical tests are provided in the "Computer code used for statistical tests" section of the Supplementary Materials.

Comparison of HC and HD groups (two-sample)

The statistical significance between the HC and HD groups was compared using both a Welch test and a permutation test. Using either P value does not change the conclusions presented in the paper. The permutation test is more appropriate given the small sample size ($n = 14$).

1) Welch test: two-sample, two-sided t test with unequal variances. The Satterthwaite's approximation was used to calculate the effective degrees of freedom.

2) Permutation test (two-sample): two-sample permutation test using Monte Carlo method with $10^5 - 1$ replications.

Comparison of a single group at two time points (paired)

When comparing the same participant group at two different time points (i.e., HCs pre versus HCs post), both a paired Student's t test and a one-sample permutation test (on the difference, i.e., $\text{diff} = \text{HC}_{\text{pre}} - \text{HC}_{\text{post}}$) were used. Using either P value does not change the conclusions presented in the paper. The permutation test is more appropriate given the small sample size ($n = 14$).

1) Permutation test (one-sample): Fisher's one-sample permutation, two-sided test with 10^5 permutations.

2) Paired t test: paired, two-sided Student's t test.

Quantile regression of pixel-wise MRI data

A quantile regression with clustering was used on the pixel-wise MRI data to quantify the difference between HC and HD groups at each time point.

Quantile regression with clustering: quantile regression with wild bootstrap method proposed by Feng *et al.* (57) to estimate SEs because the data had clustered responses (i.e., each participant has data from many pixels, which are not independent).

Determination of optimal model for T_2 data fitting

The extra sum-of-squares F test, or simply F test, was used to determine the optimal number of exponentials that should be used to model the T_2 data. The test compares two nested models where one model is a simpler version of the other. The relationship between the relative increase in sum of squares and relative increase in degrees of freedom is expressed as an F ratio

$$\text{Sum of squares} = SS = \sum_{i=1}^n (y - y_i)^2$$

$$F \text{ ratio} = \frac{(SS1 - SS2)/SS2}{(DF1 - DF2)/DF2}$$

where y is the true value of the data, y_i is the value predicted by the model, and DF , or degrees of freedom, is defined as $n - m$ where n is the number of data points and m is the number of parameters in the model. The more complex model is defined as model 2 and the simpler model is model 1.

The P value is obtained from an F distribution look-up table. The null hypothesis is that the simpler model is correct. We set our P value threshold to 0.05.

SUPPLEMENTARY MATERIALS

stm.sciencemag.org/cgi/content/full/11/502/eaau1749/DC1

Computer code for statistical tests

Fig. S1. Pixel-wise heatmap of MRI biexponential T_2 fit results.

Fig. S2. Histogram of MRI pixel-wise T_2 relaxation time values in muscular and subcutaneous tissue at baseline.

Fig. S3. Histogram of MRI pixel-wise T_2 relaxation time values in muscular tissue.

Fig. S4. Histogram of MRI pixel-wise T_2 relaxation time values in subcutaneous tissue.

Fig. S5. Histogram of MRI pixel-wise RA_{long} values in muscular tissue.

Fig. S6. Histogram of MRI pixel-wise RA_{long} values in subcutaneous tissue.

Fig. S7. CDFs of MRI pixel-wise RA_{long} values in muscular tissue.

Fig. S8. T_2 decays of phantoms measured on MRI and NMR sensor.

Fig. S9. T_2 results of phantoms measured on MRI and NMR sensor.

Fig. S10. Quantitative NMR relaxometry findings at different fluid states.

Fig. S11. Pixels deleted by the MRI pixel-wise fitting criteria.

Fig. S12. B_0 magnetic field map of the NMR sensor.

Fig. S13. NMR sensor T_2 decay signal from a representative HC and HD participant.

Table S1. Individual-level demographics of the study population.

Table S2. F test comparison of multiexponential fits for pixel-wise MRI data.

Table S3. Summary of change in pixel-wise MRI values within ROIs.

Table S4. Summary of quantile regression results for MRI pixel-wise RA_{long} values from the muscle ROI.

Table S5. Summary of MRI RA_{long} values for muscle (whole ROI average).

Table S6. Comparison of specifications of the NMR sensor with those of a traditional MRI scanner.

Table S7. Summary of phantom T_2 relaxation time results for MRI and NMR sensor.

Table S8. Summary of RA_{b} values from NMR sensor.

Table S9. Summary of RA_{long} values from MRI small voxel: Anterior 1 with subcutaneous and muscle.

Table S10. Summary of RA_{long} values from MRI small voxel: Anterior 2 with muscle only.

Table S11. Summary of RA_{long} values from MRI small voxel: Lateral 1 with subcutaneous and muscle.

Table S12. Summary of RA_{long} values from MRI small voxel: Lateral 2 with muscle only.

Table S13. Summary of whole-body R_e BI values.

Table S14. Summary of whole-body R_{inf} BI results.

Table S15. Summary of leg segmental R_e BI results.

Table S16. Summary of leg segmental R_{inf} BI results.

Table S17. Change in T_2 relaxation time of phantom measured with each human NMR sensor measurement.

REFERENCES AND NOTES

- D. Siriopol, S. Hogas, L. Voroneanu, M. Onofriescu, M. Apetrii, M. Oleniuc, M. Moscalu, R. Sascu, A. Covic, Predicting mortality in haemodialysis patients: A comparison between lung ultrasonography, bioimpedance data and echocardiography parameters. *Nephrol. Dial. Transplant.* **28**, 2851–2859 (2013).
- C. Zoccali, U. Moissl, C. Chazot, F. Mallamaci, G. Tripepi, O. Arkossy, P. Wabel, S. Stuard, Chronic Fluid Overload and Mortality in ESRD. *J. Am. Soc. Nephrol.* **28**, 2491–2497 (2017).
- C. Ekinci, M. Karabork, D. Siriopol, N. Dincer, A. Covic, M. Kanbay, Effects of volume overload and current techniques for the assessment of fluid status in patients with renal disease. *Blood Purif.* **46**, 34–47 (2018).
- D. N. Reddan, L. A. Szczech, V. Hasselblad, E. G. Lowrie, R. M. Lindsay, J. Himmelfarb, R. D. Toto, J. Stivelman, J. F. Winchester, L. A. Zillman, R. M. Califf, W. F. Owen, Intradialytic blood volume monitoring in ambulatory hemodialysis patients: a randomized trial. *J. Am. Soc. Nephrol.* **16**, 2162–2169 (2005).
- S. Ishibe, A. J. Peixoto, Methods of assessment of volume status and intercompartmental fluid shifts in hemodialysis patients: Implications in clinical practice. *Semin. Dial.* **17**, 37–43 (2004).
- M. W. Taal, G. M. Chertow, P. A. Marsden, K. Skorecki, A. S. L. Yu, B. M. Brenner, *Brenner and Rector's The Kidney* (Elsevier Health Sciences, 2011).
- L. E. Armstrong, Assessing hydration status: The elusive gold standard. *J. Am. Coll. Nutr.* **26**, 575S–584S (2007).
- A. D. Sinha, Why assistive technology is needed for probing of dry weight. *Blood Purif.* **31**, 197–202 (2011).
- R. Agarwal, M. R. Weir, Dry-weight: A concept revisited in an effort to avoid medication-directed approaches for blood pressure control in hemodialysis patients. *Clin. J. Am. Soc. Nephrol.* **5**, 1255–1260 (2010).
- C. Fallick, P. A. Sobotka, M. E. Dunlap, Sympathetically mediated changes in capacitance: Redistribution of the venous reservoir as a cause of decompensation. *Circ. Heart Fail.* **4**, 669–675 (2011).
- R. Agarwal, Volume overload in dialysis: The elephant in the room, no one can see. *Am. J. Nephrol.* **38**, 75–77 (2013).
- M. Jessup, S. Brozena, Heart Failure. *N. Engl. J. Med.* **348**, 2007–2018 (2003).
- W. Frank Peacock, K. M. Soto, Current technique of fluid status assessment. *Congest. Heart Fail.* **16**, S45–S51 (2010).
- S. R. Walsh, E. J. Cook, R. Bentley, N. Farooq, J. Gardner-Thorpe, T. Tang, M. E. Gaunt, E. C. Coveney, Perioperative fluid management: Prospective audit. *Int. J. Clin. Pract.* **62**, 492–497 (2008).
- M. Gheorghiadu, G. Filippatos, L. De Luca, J. Burnett, Congestion in acute heart failure syndromes: An essential target of evaluation and treatment. *Am. J. Med.* **119**, S3–S10 (2006).
- S. Sieck, in *Short Stay Management of Acute Heart Failure*, W. F. Peacock, Ed. (Humana Press, Totowa, NJ, 2012), pp. 9–32.
- Y. Dou, F. Zhu, P. Kotanko, Assessment of extracellular fluid volume and fluid status in hemodialysis patients: current status and technical advances. *Semin. Dial.* **25**, 377–387 (2012).
- U. G. Kyle, I. Bosaeus, A. D. De Lorenzo, P. Deurenberg, M. Elia, J. M. Gómez, B. L. Heitmann, L. Kent-Smith, J.-C. Melchior, M. Pirlich, H. Scharfetter, A. M. W. J. Schols, C. Pichard, Bioelectrical impedance analysis—Part I: review of principles and methods. *Clin. Nutr.* **23**, 1226–1243 (2004).
- C. S. Zuo, R. A. Villafuerte, M. E. Henry, R. L. Dobbins, C. Lee, Y. Sung, C. Haws, M. Butman, S. Miller, A. Manos, B. S. Orban, A. P. Brown, R. Hodge, D. J. Nunez, P. F. Renshaw, MRI assessment of drug-induced fluid accumulation in humans: Validation of the technology. *Magn. Reson. Imaging* **26**, 629–637 (2008).
- M. Dehghan, A. T. Merchant, Is bioelectrical impedance accurate for use in large epidemiological studies? *Nutr. J.* **7**, 26 (2008).
- R. Mathur-De Vré, The NMR studies of water in biological systems. *Prog. Biophys. Mol. Biol.* **35**, 103–134 (1979).
- A. Sawant, A. A. House, B. M. Chesworth, J. Gati, R. Lindsay, D. M. Connelly, R. Bartha, T. J. Overend, Reliability of calf bioelectrical impedance spectroscopy and magnetic-resonance-imaging-acquired skeletal muscle hydration measures in healthy people. *Physiol. J.* **2013**, 563494 (2013).
- F. Casanova, J. Perlo, B. Blümich, *Single-Sided NMR* (Springer, 2011).
- G. R. Coates, L. Xiao, M. G. Prammer, *NMR Logging: Principles and Applications* (Halliburton Energy Services Publication, 1999).
- D. Allen, S. Crary, R. Freedman, M. Andreani, W. Klopff, R. Badry, C. Flaum, W. Kenyon, R. Kleinberg, P. Gossenberger, J. Horkowitz, D. Logan, J. Singer, J. White, How to use borehole nuclear magnetic resonance. *Oilf. Rev. Summer*, 34–57 (1997).
- H. Todt, G. Guthausen, W. Burk, D. Schmalbein, A. Kamlowski, Water/moisture and fat analysis by time-domain NMR. *Food Chem.* **96**, 436–440 (2006).
- T. Apih, B. Rameev, G. Mozzhukhin, J. Barras, in *NATO Advanced Research Workshop on Magnetic Resonance Detection of Explosives and Illicit Materials* (Springer, 2012).
- M. C. Tourell, T. S. Ali, H. J. Hugo, C. Pyke, S. Yang, T. Lloyd, E. W. Thompson, K. I. Momot, T_1 -based sensing of mammographic density using single-sided portable NMR. *Magn. Reson. Med.* **80**, 1243–1251 (2018).
- G. Gambarota, B. E. Ciarns, C. B. Berde, R. V. Mulkern, Osmotic effects on the T_2 relaxation decay of in vivo muscle. *Magn. Reson. Med.* **46**, 592–599 (2001).

30. Z. Ababneh, H. Beloeil, C. B. Berde, G. Gambarota, S. E. Maier, R. V. Mulkern, Biexponential parameterization of diffusion and T₂ relaxation decay curves in a rat muscle edema model: decay curve components and water compartments. *Magn. Reson. Med.* **54**, 524–531 (2005).
31. E. C. A. Araujo, Y. Fromes, P. G. Carlier, New insights on human skeletal muscle tissue compartments revealed by in vivo T2 NMR relaxometry. *Biophys. J.* **106**, 2267–2274 (2014).
32. R. H. Fan, M. D. Does, Compartmental Relaxation and diffusion tensor imaging measurements in vivo in λ-carrageenan-induced edema in rat skeletal muscle. *NMR Biomed.* **21**, 566–573 (2008).
33. S. N. Ho, Intracellular water homeostasis and the mammalian cellular osmotic stress response. *J. Cell. Physiol.* **206**, 9–15 (2006).
34. M. Li, C. C. Vassiliou, L. A. Colucci, M. J. Cima, ¹H nuclear magnetic resonance (NMR) as a tool to measure dehydration in mice. *NMR Biomed.* **28**, 1031–1039 (2015).
35. D. L. Costill, B. Saltin, in *Metabolic Adaptation to Prolonged Physical Exercise*, H. Howald, J. R. Poortmans, Eds. (Birkhäuser, 1975), pp. 352–360.
36. H. Nose, T. Morimoto, K. Ogura, Distribution of water losses among fluid compartments of tissues under thermal dehydration in the rat. *Jpn. J. Physiol.* **33**, 1019–1029 (1983).
37. A. Bashyam, M. Li, M. J. Cima, Design and Experimental Validation of Unilateral Linear Halbach Magnet Arrays for Single-Sided Magnetic Resonance. *J. Magn. Reson.* **292**, 36–43 (2018).
38. R. Freedman, N. Heaton, Fluid Characterization Using Nuclear Magnetic Resonance Logging. *Petrophysics* **45**, 241–250 (2004).
39. J.-Z. Wang, R. S. Mezzrich, J. B. Kostis, The use of magnetic resonance imaging in the study of edema. *Angiology*, 358–364 (1991).
40. J. D. Meler, M. A. Solomon, J. R. Steele, C. W. Yancy Jr., R. W. Parkey, J. L. Fleckenstein, The MR appearance of volume overload in the lower extremities. *J. Comput. Assist. Tomogr.* **21**, 969–973 (1997).
41. D. Shemin, L. D. Dworkin, Sodium balance in renal failure. *Curr. Opin. Nephrol. Hypertens.* **6**, 128–132 (1997).
42. C. Ronco, *Fluid Overload: Diagnosis and Management* (Karger, 2010).
43. G. Bhawe, E. G. Neilson, Volume depletion versus dehydration: How understanding the difference can guide therapy. *Am. J. Kidney Dis.* **58**, 302–309 (2011).
44. S. Connor, J. K. Nicholson, J. R. Everett, Chemical-exchange and paramagnetic T2 relaxation agents for water suppression in spin-echo proton nuclear magnetic resonance spectroscopy of biological fluids. *Anal. Chem.* **59**, 2885–2891 (1987).
45. C. S. Zuo, R. A. Villafuerte, M. E. Henry, M. Butman, R. L. Dobbins, Y. He, B. S. Orban, K. Cayetano, L. Wang, A. P. Brown, D. J. Nunez, J. Brown, P. F. Renshaw, Proton and sodium MRI assessment of fluid level in calf tissue. *J. Magn. Reson. Imaging* **24**, 191–196 (2006).
46. H.-L. Margaret Cheng, N. Stikov, N. R. Ghugre, G. A. Wright, Practical medical applications of quantitative MR relaxometry. *J. Magn. Reson. Imaging* **36**, 805–824 (2012).
47. T. Yankeelov, D. R. Pickens, R. R. Price, *Quantitative MRI in Cancer* (CRC Press, ed. 1, 2012).
48. J. C. Wood, C. Enriquez, N. Ghugre, J. M. Tyzka, S. Carson, M. D. Nelson, T. D. Coates, MRI R2 and R2* mapping accurately estimates hepatic iron concentration in transfusion-dependent thalassemia and sickle cell disease patients. *Blood* **106**, 1460–1465 (2005).
49. B. Blümich, J. Perlo, F. Casanova, Mobile single-sided NMR. *Prog. Nucl. Magn. Reson. Spectrosc.* **52**, 197–269 (2008).
50. M. Sarraçanie, C. D. LaPierre, N. Salameh, D. E. J. Waddington, T. Witzel, M. S. Rosen, Low-cost high-performance MRI. *Sci. Rep.* **5**, 15177 (2015).
51. M. Veevaete, “Applications of Earth’s Field NMR to porous systems and polymer gels,” thesis, Universität Bremen (2008).
52. L. L. Tsai, R. W. Mair, M. S. Rosen, S. Patz, R. L. Walsworth, An open-access, very-low-field MRI system for posture-dependent 3He human lung imaging. *J. Magn. Reson.* **193**, 274–285 (2008).
53. C. Z. Cooley, J. P. Stockmann, B. D. Armstrong, M. Sarraçanie, M. H. Lev, M. S. Rosen, L. L. Wald, Two-dimensional imaging in a lightweight portable MRI scanner without gradient coils. *Magn. Reson. Med.* **73**, 872–883 (2015).
54. P. McCarthy, *FSLeyes* (2019); doi:10.5281/ZENODO.2630502.
55. K. Hattori, Y. Ikemoto, W. Takao, S. Ohno, T. Harimoto, S. Kanazawa, M. Oita, K. Shibuya, M. Kuroda, H. Kato, K. Hattori, Development of MRI phantom equivalent to human tissues for 3.0-T MRI. *Med. Phys.* **40**, 032303 (2013).
56. *HYDRA ECF/ICF (Model 4200)* (San Diego, CA, USA).
57. X. Feng, X. He, J. Hu, Wild bootstrap for quantile regression. *Biometrika* **98**, 995–999 (2011).

Acknowledgments: We thank members of the MGH Nephrology Division and Athinoula A. Martinos Center for Biomedical Imaging at MGH for their valuable feedback and help with data collection: R. Thadhani, R. Ahmed, D. Sullivan, L. White, and M. O’Hara. We thank M. Hochman for image interpretation and E. Adalsteinsson, A. Takahashi, J. Stockmann, B. Zhao, P. Garcia-Polo, M. Torriani, A. Bashyam, A. Hall, J. Lee, A. van der Kouwe, C. Cooley, L. Wald, and J. Kirsch for assistance with protocol development. We thank M. Sylvia-Reardon and the MGH Dialysis Clinic for allowing us to conduct this study amid the unit’s busy workflow. We acknowledge statistical support (statistical methods and computing resources) provided by data science specialists S. Worthington and S. Goshev at the Institute for Quantitative Social Science (IQSS) at Harvard University, as well as by the Harvard Catalyst Biostatistical Consulting services and the Koch Institute Swanson Biotechnology Center (Bioinformatics & Computing). We thank the Athinoula A. Martinos Imaging Center at the McGovern Institute for Brain Research, MIT for support. **Funding:** Support for this study was provided by the MGH-MIT Strategic Partnership Grand Challenge grant and the Air Force Medical Services/Institute of Soldier Nanotechnologies grant. L.A.C. was funded by the NSF Graduate Research Fellowships Program (GRFP). This research was carried out in part at the Athinoula A. Martinos Center for Biomedical Imaging at the MGH, using resources provided by the Center for Functional Neuroimaging Technologies (P41EB015896), a P41 Biotechnology Resource Grant supported by the National Institute of Biomedical Imaging and Bioengineering (NIBIB), National Institutes of Health. The project was supported in part by grant number 1UL1TR001102 (Partners Clinical Research Center), the Koch Institute Support (core) grant P30-CA14051 from the National Cancer Institute, Harvard Catalyst | The Harvard Clinical and Translational Science Center (National Center for Advancing Translational Sciences, National Institutes of Health Award UL1TR002541), and financial contributions from Harvard University and its affiliated academic health care centers. The content is solely the responsibility of the authors and does not necessarily represent the official views of the National Center For Research Resources, the National Center for Advancing Translational Science, Harvard Catalyst, Harvard University and its affiliated academic health care centers, or the National Institutes of Health. **Author contributions:** M.J.C., L.A.C., M.L., H.Y.L., K.M.C., and D.A.A. conceptualized the study and acquired funding. L.A.C., M.L., X.V.P., K.M.C., and A.S.A. performed data collection and/or participant screening and recruitment. L.A.C., M.L., and M.S.R. were involved in developing the technical methods (hardware and analysis). L.A.C. conducted the analysis, and K.M.C., M.S.R., D.A.A., and H.Y.L. provided feedback to shape the analysis. L.A.C. wrote the original manuscript draft, and all authors contributed to reviewing and editing. **Competing interests:** L.A.C., M.L., and M.J.C. are listed as inventors on a patent (US: 14/896,806) filed by MIT for the use of magnetic resonance in hydration monitoring. M.L. and M.J.C. are listed as inventors on a patent application (US: 15/957,429) filed by MIT covering the magnet design for the portable NMR sensor. **Data and materials availability:** All data associated with this study are present in the paper or the Supplementary Materials. Code for all data processing and analysis is available on <https://github.com/lcolucci/portable-nmr>.

Submitted 29 November 2018

Resubmitted 12 February 2019

Accepted 23 May 2019

Published 24 July 2019

10.1126/scitranslmed.aau1749

Citation: L. A. Colucci, K. M. Corapi, M. Li, X. V. Parada, A. S. Allegretti, H. Y. Lin, D. A. Ausiello, M. S. Rosen, M. J. Cima, Fluid assessment in dialysis patients by point-of-care magnetic relaxometry. *Sci. Transl. Med.* **11**, eaau1749 (2019).

Fluid assessment in dialysis patients by point-of-care magnetic relaxometry

Lina A. Colucci, Kristin M. Corapi, Matthew Li, Xavier Vela Parada, Andrew S. Allegretti, Herbert Y. Lin, Dennis A. Ausiello, Matthew S. Rosen and Michael J. Cima

Sci Transl Med 11, eaau1749.
DOI: 10.1126/scitranslmed.aau1749

Detecting fluid imbalance

The kidneys play an important role in maintaining fluid balance within the body. Patients with end-stage renal disease often experience swelling in the lower limbs due to excess extracellular fluid, and fluid status must be closely monitored during hemodialysis. Colucci and colleagues devised a portable nuclear magnetic resonance (NMR) sensor to assess tissue fluid status. Changes in extracellular fluid space in leg muscles of patients undergoing dialysis detected by the NMR sensor were similar to NMR relaxometry measured by magnetic resonance imaging. Results suggest that the nonimaging NMR sensors can provide objective, rapid bedside evaluation of fluid status in patients.

ARTICLE TOOLS

<http://stm.sciencemag.org/content/11/502/eaau1749>

SUPPLEMENTARY MATERIALS

<http://stm.sciencemag.org/content/suppl/2019/07/22/11.502.eaau1749.DC1>

RELATED CONTENT

<http://stm.sciencemag.org/content/scitransmed/11/495/eaav5341.full>
<http://stm.sciencemag.org/content/scitransmed/10/456/eaam6474.full>
<http://stm.sciencemag.org/content/scitransmed/3/71/71ra16.full>
<http://stm.sciencemag.org/content/scitransmed/4/141/141ra92.full>

REFERENCES

This article cites 45 articles, 5 of which you can access for free
<http://stm.sciencemag.org/content/11/502/eaau1749#BIBL>

PERMISSIONS

<http://www.sciencemag.org/help/reprints-and-permissions>

Use of this article is subject to the [Terms of Service](#)